Check for updates

AGU ADVANCING EARTH AND SPACE SCIENCE

Geophysical Research Letters

RESEARCH LETTER
10.1029/2020GL091613

On the Origin of Donut-Shaped Electron Distributions Within Magnetic Cavities

Jing-Huan Li[1], Xu-Zhi Zhou[1], Qiu-Gang Zong[1], Fan Yang[1], Suiyan Fu[1], Shutao Yao[2], Ji Liu[3], and Quanqi Shi[2]

[1]School of Earth and Space Sciences, Peking University, Beijing, China, [2]Institute of Space Sciences, Shandong University, Weihai, China, [3]Department of Physics, University of Alberta, Edmonton, Canada

Key Points:

- Magnetic cavity electrons sometimes display donut-shaped pitch angle distributions, which differ from their usual, 90°-concentrated form
- Numerical simulations show that donut-shaped electron distributions originate from the shrinkage and deepening of magnetic cavities
- The donut-shaped distributions are formed by the combined effects of betatron cooling, radial transport, and pitch angle variations

Supporting Information:

- Supporting Information S1

Correspondence to:
X.-Z. Zhou,
xzzhou@pku.edu.cn

Citation:
Li, J.-H., Zhou, X.-Z., Zong, Q.-G., Yang, F., Fu, S., Yao, S., et al. (2021). On the origin of donut-shaped electron distributions within magnetic cavities. *Geophysical Research Letters*, *48*, e2020GL091613. https://doi.org/10.1029/2020GL091613

Received 6 NOV 2020
Accepted 10 DEC 2020

Abstract Magnetic cavities, also known as magnetic holes, are ubiquitous in space plasmas characterized by depressed magnetic strength and enhanced plasma pressure. Most of the observed cavities are associated with anisotropic particle distributions with higher fluxes in the direction perpendicular to the magnetic field. Recent observations of kinetic-scale magnetic cavities have identified another type of electron distributions in the pitch angle spectrum, the so-called donut-shaped distributions, although their formation mechanism remains unclear. Here, we present a simplistic model of cavity shrinkage and deepening, in which electrons are traced backward in time to the initial, equilibrium-state cavity. The resulting electron distributions, determined from Liouville's theorem, agree with the observations in the presence of donut-shaped pitch angle structures. The model also enables a quantitative evaluation on the roles of betatron cooling, radial transport, and pitch angle variations in the formation of donut-shaped electron distributions within evolving magnetic cavities.

Plain Language Summary Satellite observations of the space plasma environments have identified many localized structures with reduced magnetic field amplitude in an otherwise unperturbed background. These structures, referred to as magnetic cavities or holes, are usually observed in association with anisotropic particle distributions, with higher fluxes in the direction perpendicular to the magnetic field. It is these anisotropic distributions that provide the strongest support to the prevalent understanding that magnetic cavities are generated via mirror or electron-mirror instabilities. However, recent observations have identified a different type of electron distributions in kinetic-scale magnetic cavities, the so-called donut-shaped distributions after their characteristic appearances in the electron pitch angle spectrum. In this paper, we examine the hypothesis that donut-shaped electron distributions originate from the simultaneous deepening and shrinkage of magnetic cavities, a process identified in recent observations. To do so, we carry out a particle-tracing simulation to analyze the electron behavior within the evolving magnetic cavity, which includes the adiabatic betatron cooling, radial transport, and pitch angle variations. The variations of the electron phase space densities are then computed based on Liouville's theorem, which results in donut-shaped distributions consistent with observations from NASA's Magnetospheric Multiscale mission.

1. Introduction

Magnetic cavities, also referred to as magnetic holes, are quasisymmetric structures with depressed magnetic strength and enhanced plasma pressure. These structures, with size varying from fluid down to electron kinetic scales, have been reported in various space environments including magnetotail (Balikhin et al., 2012; Ge et al., 2011; Goodrich et al., 2016; Shustov et al., 2019; Sun et al., 2012; Sundberg et al., 2015; Zhang et al., 2017), magnetosheath (H. Liu et al., 2019b; Tsurutani et al., 2011; Yao et al., 2017), solar wind (Turner et al., 1977; Winterhalter et al., 1994; Xiao et al., 2010), heliosheath (Burlaga et al., 2006), and planetary/cometary environments (Cattaneo et al., 1998; Joy et al., 2006; Plaschke et al., 2018; Russell et al., 1987).

The magnetic cavity generation is often attributed to the mirror (Ge et al., 2011; Kivelson & Southwood, 1996; Winterhalter et al., 1994) or electron-mirror instabilities (Hellinger & Stverak, 2018; Yao et al., 2019). This hypothesis is supported by observations of anisotropic particle distributions within magnetic cavities, with higher fluxes perpendicular to the magnetic field than in the parallel direction (Gershman et al., 2016; Winterhalter et al., 1994). It is the diamagnetic motion of the perpendicular-moving particles that contributes

© 2020. American Geophysical Union. All Rights Reserved.

to the ring-shaped azimuthal current and consequently causes the magnetic depression within the cavity (Haynes et al., 2015; Yao et al., 2017; Zhang et al., 2017).

Kinetic models of equilibrium-state magnetic cavities have been proposed by solving the Vlasov–Maxwell equations in cylindrical coordinates (Li et al., 2020; Shustov et al., 2016). In these models, the Vlasov equation is satisfied by constructing the particle distributions as functions of invariants of motion, including the particle energy and the canonical angular momentum in the azimuthal direction. In Li et al. (2020), the magnetic moment is considered another invariant of motion, which enables particle anisotropy and nongyrotropy within the cavity. The constructed particle distributions are then substituted into Maxwell's equations, to determine the field and plasma profiles self-consistently. The Li et al. (2020) model has been also applied to an event of nested magnetic cavities, and the excellent agreement between the model and spacecraft observations supports the scenario of quasistationary magnetic cavity emergence in turbulent plasmas (Haynes et al., 2015; Roytershteyn et al., 2015).

The dominance of perpendicular-moving particles, however, may not be ever present in every cavity. Recent observations have identified another kind of anisotropic electron distributions, referred to as donut-shaped distributions after their characteristic appearances in the pitch angle spectrum of kinetic-scale cavities (Yao et al., 2018). Figure 1 shows the observational overview of the event. Although the detailed descriptions will be given in the next section, we point out here that the donut-shaped distributions can be clearly seen in the zoomed-in spectrum of Figures 1(l) and 1(m). The perpendicular-moving electrons dominated near the cavity edges (with a sharp gradient of magnetic strength), whereas in the center, the fluxes peaked at intermediate pitch angles around 60°/120°. It has been speculated in Yao et al. (2018) that donut-shaped distributions could result from betatron cooling (Chisham et al., 1998) process associated with the cavity deepening (i.e., the decreasing of magnetic strength with time). This speculation, although qualitative and inconclusive, has been supported by an observational case study (Ahmadi et al., 2018), in which donut-shaped electron distributions were observed only in deep magnetic cavities, whereas in shallow cavities the electrons were concentrated around 90° pitch angles.

Note that magnetic cavities may experience different kinds of dynamic evolution other than deepening, most noteworthy the shrinking process (H. Liu et al., 2019a; Yao et al., 2020). In fact, recent observations have identified simultaneous occurrence of cavity deepening and shrinkage (J. Liu et al., 2020), which explains the statistical anticorrelation between the spatial scale and depression depth of magnetic cavities (Yao et al., 2017). In this study, we consider simultaneous deepening and shrinkage of magnetic cavities, and simulate the evolution of electron distributions during this process. As we will show, the simulated electron distributions gradually evolve from the 90°-concentrated spectrum toward the donut-shaped spectrum, which agrees with the observations and provides quantitative insights into the underlying electron dynamics.

2. Observations

We next revisit the Yao et al. (2018) event on September 10, 2015, in which a series of kinetic-scale magnetic cavities were successively observed in the dusk side magnetosheath by the Magnetospheric Multiscale (MMS) spacecraft at GSE [1.7, 11.5, −0.5] R_E. The MMS mission (Burch et al., 2016), consisting of four closely separated spacecraft (MMS1–MMS4), enables us to analyze the electron distributions with unprecedented high resolution (30 ms) from the Fast Plasma Investigation instrument (Pollock et al., 2016). The magnetic field data utilized are obtained from the FIELDS instrument (Torbert et al., 2016).

Figure 1 presents the MMS1 observations of many kinetic-scale magnetic cavities. The ion and electron energy spectra, given in Figures 1(a) and 1(b), are consistent with the characteristics of magnetosheath plasmas. Typical signatures of magnetic cavities, including the depressed magnetic strength, the enhanced plasma density, and the enhanced electron temperature, are shown in Figures 1(c)–1(e), respectively. During this interval, the magnetic field direction hardly changed from the $-z$ direction in GSE coordinates, and the ion bulk velocity in Figure 1(f) remained nearly constant. Based on these observations, a local *LMN* coordinate system is defined, in which the *L* direction ([0.05, −0.10, −0.99] GSE) is the average magnetic field direction, *M* direction ([0.57, 0.82, −0.06] GSE) is determined from the cross product of *L* and the average ion bulk velocity, and *N* direction ([0.82, −0.56, 0.10] GSE) completes the triad. Figures 1(g) and 1(h) show

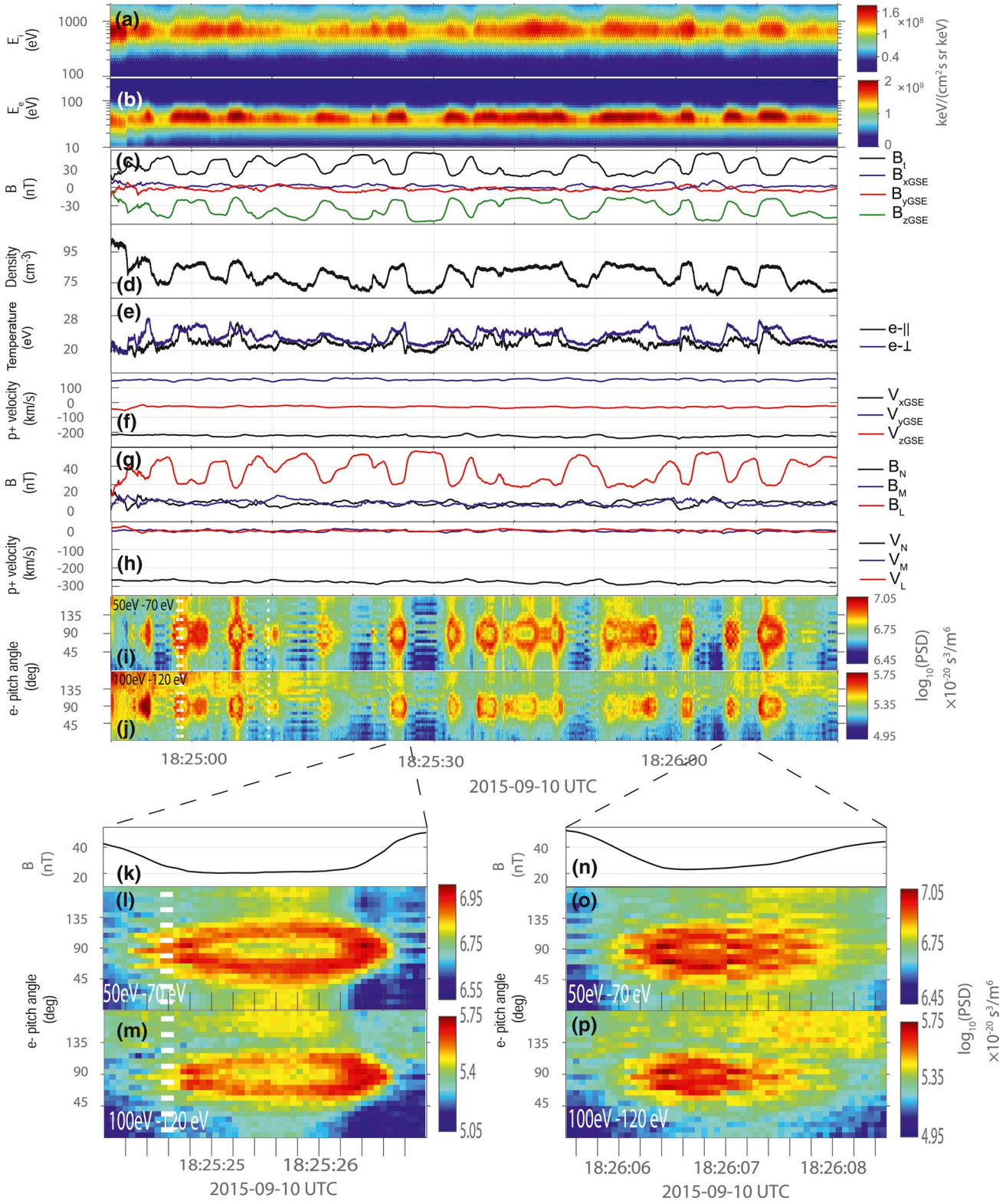

Figure 1. A 90-s event overview of the magnetic cavities observed by MMS1 spacecraft on September 10, 2015. (a, b) Energy spectrograms of ion and electron fluxes, respectively. (c) Magnetic field in GSE coordinates. (d) Plasma density. (e) Electron temperatures. (f) Ion bulk velocity in GSE coordinates. (g, h) Magnetic field and ion bulk velocity in the defined local *LMN* coordinates. (i, j) Electron pitch angle distributions (PADs) in the 50–70 eV and 100–120 eV energy channels. (k–p) Zoomed-in view of two magnetic cavities, observed from 1825:24 UT to 1825:27 UT and from 1826:05.5 UT to 1826:08.5 UT, respectively. The three panels are the corresponding magnetic strength and PADs.

the magnetic field and the ion bulk velocity in the *LMN* coordinates, respectively. The nearly constant ion bulk velocity, approximately 270 km/s in the $-N$ direction, agrees with the common understanding that magnetic cavities are nonpropagating structures in the ion fluid rest frame (Haynes et al., 2015). In this frame, the MMS1 spacecraft moved across the series of immobile cavities along the $+N$ direction, and its 3-s traversal time across a typical cavity indicates the spatial scale of ~800 km.

Figures 1(i) and 1(j) show the pitch angle spectra of electron phase space densities (PSDs) within the 50–70 eV and 100–120 eV energy channels, respectively. One can clearly see that many magnetic cavities were associated with donut-shaped electron distributions. The zoomed-in view of a typical cavity between 1825:24 and 1825:27 UT, given in Figures 1(k)–1(m), shows that the perpendicular-moving electron PSDs in the cavity center were lower than those at intermediate pitch angles around 60° or 120°, whereas the electron PSDs near the cavity edges peaked in the perpendicular direction. Moreover, the perpendicular-moving electron PSDs were lower in the cavity center than the edges. The donut-shaped distributions were also manifested by the electron temperature variations (see Figure 1(e)), with comparable perpendicular and parallel temperatures within the center (due to the peaked PSDs at intermediate pitch angles) and higher perpendicular temperatures near the edges.

Note that even in this event, there were also magnetic cavities with the absence of donut-shaped electron distributions. An example is given in Figures 1(n)–1(p), which provide the zoomed-in view of the cavity between 18:26:05.5 and 18:26:08.5 UT when the electron PSDs peaked in the perpendicular direction. Similar distributions are also found in other cavities, for example, near 1825:01 and 1825:10 UT (see Figures 1(i) and 1(j)). The 90°-concentrated distributions, as discussed before, are more typical in previous observations of magnetic cavities even if they appeared less frequently than the donut-shaped distributions in this event.

To examine the hypothesis that donut-shaped electron distributions evolve from the more typical, 90°-concentrated distributions during the shrinkage and deepening of magnetic cavities, we next utilize the Li et al. (2020) model to construct an equilibrium cavity with enhanced PSDs in the perpendicular direction, which provides the initial condition for particle-tracing simulation. Detailed information on the simulation and the resulting electron distributions will be presented in the next section.

3. Simulation

Our approach to simulate the evolution of electron distributions is based on Liouville's theorem (e.g., Marchand, 2010; Zhou et al., 2012). The first step, as discussed before, is to construct the initial electron distributions $f_0(\boldsymbol{r},\boldsymbol{v},t_0)$ in the six-dimensional phase space and the associated electromagnetic profiles from the self-consistent equilibrium model (Li et al., 2020). We next assume that the initial electromagnetic profile remains unchanged, except for a superposition of prescribed field perturbations to represent the cavity shrinkage and deepening process. To obtain the electron distributions $f(\boldsymbol{r},\boldsymbol{v},t)$ at any time and location, we trace the electron trajectories backward in time to identify their initial location $\boldsymbol{r}_0$ and velocity $\boldsymbol{v}_0$ within the equilibrium model at $t = t_0$. According to Liouville's theorem, $f(\boldsymbol{r},\boldsymbol{v},t)$ should be equal to $f_0(\boldsymbol{r}_0,\boldsymbol{v}_0,t_0)$. Note that although the particle-tracing approach provides an easier (than the sophisticated particle-in-cell simulations) way to understand the electron dynamics associated with external field variations, it is not self-consistent in that the simulated electron distributions cannot contribute to the prescribed field evolution. For example, the electrons within the deepening cavity would experience a betatron cooling process (as we will show later on), which according to Southwood and Kivelson (1993) would reduce the plasma pressure and restrict the field lines from moving further apart. This feedback cannot be taken into account in our simulation. In other words, we only aim to understand the evolution of electron distributions as a response to the external driver of cavity shrinkage and deepening, with no attempt to analyze how this driver appears and maintains.

The Li et al. (2020) equilibrium, adopted to construct the initial profiles of the magnetic cavity in cylindrical coordinates (ρ, φ, z), is developed based on three invariants of particle motion, including the particle energy H_α (where subscript $\alpha = i, e$ stands for ion and electrons), the canonical angular momentum $P_{\varphi\alpha}$ in the azimuthal direction, and the magnetic moment μ_e (for electrons only, since μ_i may vary within the small-scale cavity). To satisfy the Vlasov equation, the ion and electron distributions are expressed as functions of these invariants,

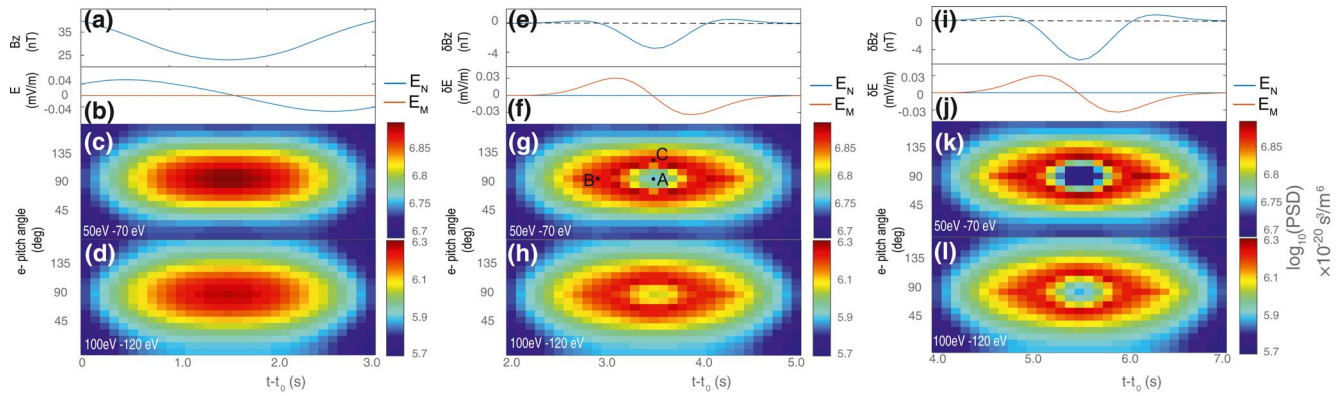

Figure 2. Virtual spacecraft observations across the equilibrium magnetic cavity (left panels) and the evolving cavity, from $t_0 + 2$ s to $t_0 + 5$ s (middle panels) and from $t_0 + 4$ s to $t_0 + 7$ s (right panels). (a, b) Modeled magnetic and electric fields. (c, d) Electron PADs in the 50–70 eV and 100–120 eV energy channels. (e–h) Virtual spacecraft vs1 observations of the perturbed magnetic field, electric field, and electron PADs, respectively. (i–l) Virtual spacecraft vs2 observations in the same format as in (e)–(h). PAD, pitch angle distribution.

$$f_e = \delta N\left(\frac{M_e}{2\pi\theta_{e,0}}\right)^{3/2}\exp\left(-\frac{H_e}{\theta_{e,0}}\right) + (1-\delta)N\left(\frac{M_e}{2\pi\theta_{e,1}}\right)^{3/2}\exp\left(-\frac{H_e - \Omega_e P_{\varphi e} + b_e\mu_e}{\theta_{e,1}}\right) \quad (1)$$

$$f_i = \delta N\left(\frac{M_i}{2\pi\theta_{i,0}}\right)^{3/2}\exp\left(-\frac{H_i}{\theta_{i,0}}\right) + (1-\delta)N\left(\frac{M_i}{2\pi\theta_{i,1}}\right)^{3/2}\exp\left(-\frac{H_i - \Omega_i P_{\varphi i}}{\theta_{i,1}}\right) \quad (2)$$

both of which are composed of a background (the first right-hand-side terms in Equations 1 and 2, independent of $P_{\varphi\alpha}$) and a current-carrying (the second terms, depending on $P_{\varphi\alpha}$) population. In this model, the magnetic field is always along the axial direction z or equivalently the L direction as defined observationally. The model parameters, designated to resemble the cavity in Figures 1(n)–1(p), include the nominal plasma density $N = 87$ cm^{-3}, the density share of the background population $\delta = 0.4$, the angular bulk velocity $\Omega_e = 0.0169$ s^{-1} and temperature $\theta_{e,1} = 30$ eV of the current-carrying electrons, the temperature $\theta_{e,0} = 20$ eV of the background electrons, the angular bulk velocity $\Omega_i = 0$ and temperature $\theta_{i,1} = 255$ eV of the current-carrying ions, the temperature $\theta_{i,0} = 205$ eV of the background ions, and the anisotropy index $b_e = -6$ nT of the current-carrying electrons (according to Equation 1, the negative b_e value indicates a higher perpendicular than parallel temperature, see Li et al. [2020] for details). Here, the selection of $\Omega_i = 0$ indicates that electrons are the only current carriers. The modeled cavity, if observed by a virtual spacecraft (hereinafter referred to as vs1) moving along the $+N$ direction at 270 km/s (the observed ion bulk velocity, see Figure 1(f)), would be manifested in Figures 2(a)–2(d) by depressed magnetic field, radially inward electric field, and 90°-concentrated electron distributions. These virtual signatures are similar to MMS1 observations in Figures 1(n)–1(p), although for generality purposes, the vs1 trajectory is slightly displaced from the cavity center by 10 km in the $+M$ direction (see Figure 3(a) for an illustration of the vs1 trajectory across the cavity).

We next construct a simple model of electromagnetic field perturbations to represent the cavity shrinkage and deepening, which require gradual decrease and increase of the magnetic strength at locations near the cavity center and the edges, respectively. Therefore, we assume that the magnetic field remains unchanged at a fixed radial distance $\rho = R_0$, and the perturbed magnetic vector potential is

$$\delta A_\varphi(\rho,t) = -\frac{\delta E_0 \rho t}{R_0}\cdot\exp\left(-\rho^2 / R_0^2\right), \quad (3)$$

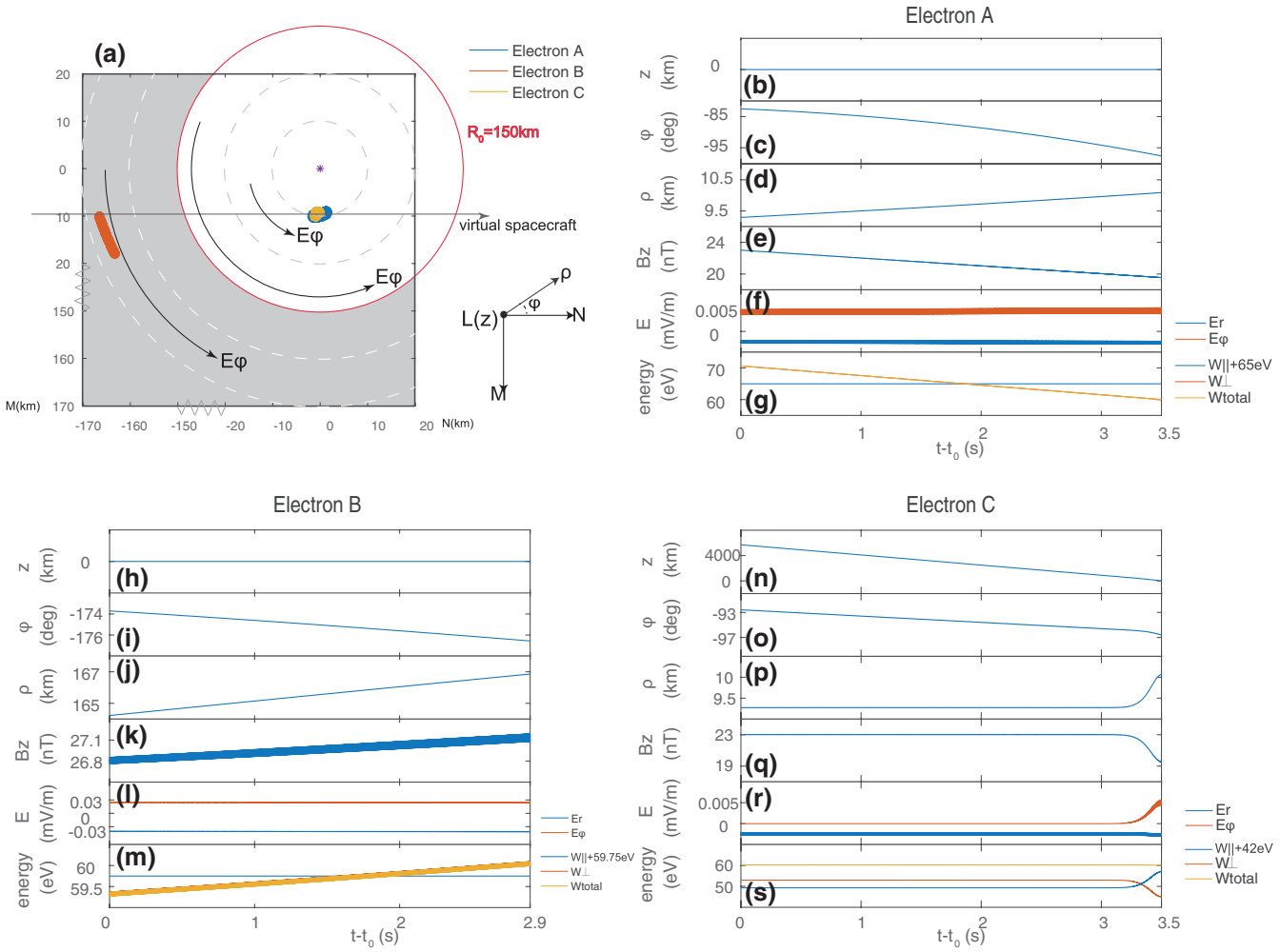

Figure 3. Trajectories of three test electrons in the shrinking/deepening magnetic cavity. (a) The *MN* projections of the electron trajectories within the cavity. The gray color denotes the $\rho > R_0$ region, in which the magnetic field increases with time. The arrows represent the azimuthal electric field. The local *LMN* and cylindrical (ρ, φ, z) coordinates are given in the bottom-right corner. Time variations of electron A's (b) z coordinate, (c, d) guiding-center φ and ρ locations, (e, f) magnetic and electric field experienced, and (g) kinetic energy. (h–m) and (n–s) are in the same format as in (b)–(g), for electrons B and C, respectively.

which corresponds to the field perturbations given by

$$\delta E_{\varphi}(\rho) = \frac{\delta E_0 \rho}{R_0} \cdot \exp\left(-\rho^2 \,/\, R_0^2\right), \tag{4}$$

$$\delta B_z(\rho, t) = \frac{2\delta E_0\left(\rho^2 - R_0^2\right)}{R_0^3} \cdot \exp\left(-\rho^2 \,/\, R_0^2\right) \cdot t, \tag{5}$$

where δE_0 regulates the cavity deepening rate or equivalently the amplitude of the induced azimuthal electric field. This assumption enables linear increase and decrease of the magnetic field with time at $\rho < R_0$ and $\rho > R_0$, respectively, with the decreasing rate approaching zero at $\rho \to +\infty$. The electric field δE_{φ}, on the other hand, is time independent and has a unipolar profile with radial distance (which peaks at $\rho = \sqrt{2}$ $R_0/2$ and approaches zero at $\rho = 0$ or $\rho \to +\infty$). These features agree with our expectation for a shrinking and deepening cavity.

One may also introduce a spatial scale of the perturbed field along the axial direction, by multiplying Equation 3 with a Gaussian envelope, to have

$$\delta A_\varphi(\rho,z,t) = -\frac{\delta E_0 \rho t}{R_0} \cdot \exp\left(-\rho^2 / R_0^2\right)\exp\left(-z^2 / Z_0^2\right), \tag{6}$$

The associated electromagnetic field perturbations are given by

$$\delta E_\varphi(\rho,z) = \frac{\delta E_0 \rho}{R_0} \cdot \exp\left(-\rho^2 / R_0^2\right)\exp\left(-z^2 / Z_0^2\right), \tag{7}$$

$$\delta B_z(\rho,z,t) = \frac{2\delta E_0\left(\rho^2 - R_0^2\right)}{R_0^3} \cdot \exp\left(-\rho^2 / R_0^2\right)\exp\left(-z^2 / Z_0^2\right) \cdot t, \tag{8}$$

$$\delta B_r(\rho,z,t) = -\frac{2\delta E_0 \rho z}{R_0^2 Z_0} \cdot \exp\left(-\rho^2 / R_0^2\right)\exp\left(-z^2 / Z_0^2\right) \cdot t, \tag{9}$$

where Z_0 represents the spatial scale along z. The modeled electromagnetic fields in the $z = 0$ plane (with the greatest cavity deepening rate) are the same as in the z-independent model, whereas at other locations, the magnetic field perturbations have not only the axial component but also the radial component. The configuration of the z-dependent shrinkage is similar to that in the magnetic mirror structures (see Yao et al., 2018, Figure 5 for a schematic view), in which the magnetic z-gradient must be accompanied by radial field to fulfill the divergence-free requirement.

In our simulation, we adopt the following parameters: $\delta E_0 = 0.075$ mV/m, $R_0 = 150$ km, and $Z_0 = 300$ km. Figures 2(e) and 2(f) present the perturbed electromagnetic fields observed by the virtual spacecraft vs1 across the shrinking cavity from $t_0 + 2$ s to $t_0 + 5$ s, in which the perturbed δB_z is negative near the cavity center and positive near the edges. Here, the radial magnetic field δB_r is zero since vs1 is confined within the $z = 0$ plane. The unipolar profile of the azimuthal electric field δE_φ is manifested in the *LMN* coordinates as bipolar δE_M variations shown in Figure 2(f). Note that the temporal scale of the field evolution (a few seconds) is larger than the electron gyroperiod (~1 ms) and lower than the drift period (hundreds of seconds) of thermal electrons around the cavity center, indicating the electron adiabatic motion with the magnetic moment conserved.

After the perturbed electromagnetic fields are superposed over the initial equilibrium, we carry out the particle-tracing procedure to determine the electron distributions at any time and location. The virtual observations of electron distributions from the vs1 spacecraft are shown in Figures 2(g) and 2(h), which present the donut-shaped pitch angle spectra of electron PSDs in both the 50–70 eV and 100–120 eV channels. These virtual observations are similar to the MMS1 observations in Figures 1(l) and 1(m), with electron PSDs maximizing at 90° and 60°/120° pitch angles near the cavity center and the edges, respectively. As the cavity keeps shrinking and deepening, the donut-shaped distributions become more prominent, as can be seen in Figures 2(i)–2(l) for virtual observations of a trailing spacecraft (referred to as vs2) that follows vs1 to traverse the cavity from $t_0 + 4$ s to $t_0 + 7$ s.

The similarity between MMS1 and virtual observations supports the hypothesis that donut-shaped electron distributions originate from cavity shrinkage and deepening. The simulation also provides an opportunity to quantitatively analyze the electron dynamics underlying their evolving distributions. To understand these variations, however, it is essential to first examine the equilibrium model for properties of the initial electron distributions and their gradients in the six-dimensional phase space. In the position space, the electron PSD (see Equation 1, or Li et al. [2020] for details) decreases with ρ and is independent of φ or z. In the velocity space, the more complicated electron distributions can be approximated by the superposition of a Maxwellian and a slightly shifted bi-Maxwellian components. Given the very low bulk velocity, the electron PSD in the energy range of interest (50–120 eV) decreases monotonically with energy in both perpendicular and parallel directions. These properties indicate that the time variations of electron distributions must be attributed either to the electron radial transport (given the negative $\partial f_e / \partial \rho$ values, the inward and outward motion would correspond to decreasing and increasing electron PSDs, respectively) or to the energy variations (with electron acceleration and deceleration associated with increasing and decreasing

PSDs, respectively). Moreover, the pitch angle variations toward or away from 90° (even if the energy remains unchanged) may also contribute to the decreasing or increasing electron PSDs, respectively. This is because, in the equilibrium cavity, the anisotropic electron distributions with higher perpendicular than parallel temperatures indicate that the energy gradients of the PSD are sharper in the parallel than in the perpendicular directions.

We next display in Figure 3 the trajectories of three typical electrons (labeled A–C) within the evolving magnetic cavity before they reach vs1 at the energy of 60 eV. The time of spacecraft encounter for the three electrons, together with their pitch angles and corresponding PSDs within the donut-shaped structure, is given in Figure 2(g). Here, electron A represents the perpendicular-moving electrons near the cavity center with decreasing PSDs (compare Figures 2(c) and 2(g)). Electron B represents the perpendicular-moving electrons at locations farther away from the center (with $\rho > R_0$), with the associated PSDs increasing slightly with time to exceed those near the center. Finally, electron C represents the population with intermediate pitch angles near the center, with higher PSDs than those perpendicular-moving electrons.

Electron A's trajectory is shown in Figure 3(a) as the blue line, which is essentially the superposition of a high-frequency, anticlockwise gyration over the slower drift motion in the clockwise and radially outward direction. Here, the outward $E \times B$ drift is associated with the induced δE_φ (see Equation 7), and the clockwise drift is caused by the higher velocity of the grad-B drift (associated with the radially outward magnetic gradient) than the anticlockwise $E \times B$ drift (caused by the radially inward Hall electric field in the equilibrium model, see Li et al. [2020]). The outward-and-clockwise drift can be also seen in Figures 3(b)–3(d), which shows the test electron's guiding-center locations before it reaches vs1. Figures 3(e) and 3(f) present the electromagnetic fields experienced by electron A, in which one can see the decreasing B_z and the weak, inward-and-anticlockwise electric field (with the high-frequency oscillations associated with electron gyration). Despite the outward-and-clockwise drift being opposite to the electric field direction, the electron kinetic energy decreases from 70 eV to 60 eV within 3.5 s (Figure 3(g)). The deceleration is caused by the electron gyration within the curled electric field induced from the decreasing magnetic field, namely, the betatron cooling process. It is this adiabatic deceleration, together with the negative PSD gradients over perpendicular energy, that dominates the electron PSD decrease near the cavity center. For the sake of completeness, we note that the decreasing trend of the electron PSDs could be compensated by the electron outward motion in association with negative $\partial f_e / \partial \rho$ values, although the latter effect is weak near the center and can hardly change the overall picture.

We next focus on electron B's trajectory, the orange line near the edges in Figure 3(a). Like electron A, this electron also drifts clockwise and outward, which can be better visualized from the time variations of its guiding center in Figures 3(h)–3(j). The electromagnetic fields experienced by electron B, shown in Figures 3(k) and 3(l), are in the same direction as those experienced by electron A, although a major difference is that the magnetic field in Figure 3(k) gradually increases. This is because electron B's radial distance is larger than R_0 (see Figure 3(a)). It is the increasing magnetic strength that causes the adiabatic betatron acceleration (see Figure 3(m) for the energy variations), which contributes to the gradual PSD enhancement near the edges that eventually exceeds those in the center. Besides, the PSD enhancement is also contributed by the electron outward drift given the negative $\partial f_e / \partial \rho$ values in the equilibrium. This effect is more important for electron B than for A since the absolute value of $\partial f_e / \partial \rho$ and the outward drift speed are both larger near the edges than in the center.

Finally, electron C's trajectory is different from the above two in that it is not confined in the $z = 0$ plane, and its projection into the plane is shown in Figure 3(a) as the yellow line. The electron's guiding-center locations, the experienced electromagnetic fields, and its perpendicular and parallel energy variations are shown in Figures 3(n)–3(s), respectively. At $t = t_0$, the electron is located ~5,000 km from the $z = 0$ plane and hardly observes any discernible field perturbations. As the electron moves along the axial direction toward the spacecraft, at $t = t_0 + 3.2$ s, it starts to experience a decreasing magnetic field and an increasing, anticlockwise electric field. From then on, the electron's perpendicular motion is similar to electron A's, albeit with lower perpendicular energy and consequently, a smaller gyroradius and a lower drift speed. Therefore, its kinetic energy also decreases (see Figure 3(s)) via betatron cooling, which could slightly reduce the associated electron PSDs. However, this process becomes more complicated by the transition between perpendicular and parallel energies (see Figure 3(s)), which is caused by the magnetic mirror force (essen-

tially the axial component of the Lorentz force in the presence of δB_r) as the electron moves along the field line toward a region with weaker magnetic strength. Given that the energy gradients of the electron PSD are larger in the parallel than in the perpendicular direction, the transition from perpendicular to parallel energy indicates a PSD enhancement. This effect dominates over the betatron cooling effect, to increase the electron PSDs at intermediate pitch angles so that the donut-shaped structures can be formed.

The above analysis suggests that donut-shaped electron distributions could be formed by the combination of betatron acceleration/deceleration, radial transport, and pitch angle variations associated with localized shrinkage and deepening of magnetic cavities. In this event, the betatron cooling effect plays a dominant role in reducing the PSDs for perpendicular-moving electrons near the cavity center, whereas the mirror force and the associated pitch angle variations are most important in enhancing the PSDs at intermediate pitch angles. To highlight the importance of the mirror force, we carry out another simulation based on the z-independent model of field evolution (Equations 3–5, in which the mirror force is absent). The results are presented in Figure S1, which shows the decrease of electron PSDs near the cavity center (due to the betatron cooling effect) at all pitch angles. The absence of donut-shaped structures indicates that betatron cooling alone is insufficient to generate the donut-shaped structures, although the relative importance of these effects in changing the electron distributions may also depend on the PSD gradients in the equilibrium cavity.

Note that the above analysis is carried out for virtual spacecraft traversing the cavity near its center. Also, the spacecraft is confined within the $z = 0$ plane (where the field perturbations maximize). In real observations, however, the spacecraft could follow different trajectories, either through the edges or displaced in the axial direction. Therefore, one should examine whether the donut-shaped distributions are typical along different spacecraft trajectories, which becomes even more important given the presence of donut-shaped distributions in most of the magnetic cavities observed in Figure 1. To do so, we launch a series of virtual spacecraft traversing the evolving cavity along different trajectories (displaced with different distances from the center in the M and/or z directions), and the resulting pitch angle spectra are displayed in Figure S2. The high probability of observing the donut-shaped electron structures is consistent with the observations that most magnetic cavities in Figure 1 were associated with donut-shaped electron distributions.

4. Conclusions

In summary, we carry out test-particle, Liouville simulations to examine the hypothesis that donut-shaped electron distributions in many magnetic cavities (Ahmadi et al., 2018; Yao et al., 2018) evolve from the more typical, 90°-concentrated distributions during the cavity shrinkage and deepening process. The simulation results agree with MMS observations, which supports this hypothesis and enables a quantitative analysis on the underlying physics. It is shown that near the cavity center, the PSD reduction for perpendicular-moving electrons is mostly attributed to the adiabatic betatron cooling effect, whereas for electrons with intermediate pitch angles (~60°/120°), the mirror force-induced transition between perpendicular and parallel energies dominates to increase the corresponding PSDs. At farther distances from the cavity center, the PSD increase is caused by betatron acceleration associated with the gradual enhancement of magnetic strength. Another factor that may change the electron PSDs is the electron radial motion associated with the induced azimuthal electric field, although this effect is less significant in our simulated formation of donut-shaped electron distributions.

Data Availability Statement

The code that the authors developed for test-particle simulations, together with a brief readme instruction, is available from the Zenodo repository (https://doi.org/10.5281/zenodo.4304598).

Acknowledgments
This study was supported by NSFC grants 41774168 and 41421003. We are grateful to the MMS team for providing the high-quality observational data utilized in this study, which are available from the MMS science data center (https://lasp.colorado.edu/mms/sdc/public/).

References

Ahmadi, N., Wilder, F. D., Ergun, R. E., Argall, M., Usanova, M. E., Breuillard, H., et al. (2018). Generation of electron whistler waves at the mirror mode magnetic holes: MMS observations and PIC simulation. *Journal of Geophysical Research: Space Physics*, *123*, 6383–6393. https://doi.org/10.1029/2018JA025452

Balikhin, M. A., Sibeck, D. G., Runov, A., & Walker, S. N. (2012). Magnetic holes in the vicinity of dipolarization fronts: Mirror or tearing structures? *Journal of Geophysical Research*, *117*, A08229. https://doi.org/10.1029/2012JA017552

Burch, J. L., Moore, T. E., Torbert, R. B., & Giles, B. L. (2016). Magnetospheric multiscale overview and science objectives. *Space Science Reviews*, *199*, 5–21. https://doi.org/10.1007/s11214-015-0164-9

Burlaga, L. F., Ness, N. F., & Acuna, M. H. (2006). Trains of magnetic holes and magnetic humps in the heliosheath. *Geophysical Research Letters*, *33*, L21106. https://doi.org/10.1029/2006GL027276

Cattaneo, M. B. B., Basile, C., Moreno, G., & Richardson, J. D. (1998). Evolution of mirror structures in the magnetosheath of Saturn from the bow shock to the magnetopause, *Journal of Geophysical Research*, *103*, 11961–11972, https://doi.org/10.1029/97JA03683

Chisham, G., Burgess, D., Schwartz, S. J., & Dunlop, M. W. (1998). Observations of electron distributions in magnetosheath mirror mode waves. *Journal of Geophysical Research*, *103*, 26765–26774. https://doi.org/10.1029/98JA02620

Ge, Y. S., McFadden, J. P., Raeder, J., Angelopoulos, V., Larson, D., & Constantinescu, O. D. (2011). Case studies of mirror-mode structures observed by THEMIS in the near-Earth tail during substorms. *Journal of Geophysical Research*, *116*, A01209. https://doi.org/10.1029/2010JA015546

Gershman, D. J., Dorelli, J. C., Viñas, A. F., Avanov, L. A., Gliese, U., Barrie, A. C., et al. (2016). Electron dynamics in a subproton-gyroscale magnetic hole. *Geophysical Research Letters*, *43*, 4112. https://doi.org/10.1002/2016GL068545

Goodrich, K. A., Ergun, R. E., Wilder, F. D., Burch, J., Torbert, R., Khotyaintsev, Y., et al. (2016). MMS multipoint electric field observations of small-scale magnetic holes. *Geophysical Research Letters*, *43*, 5953–5959. https://doi.org/10.1002/2016GL069157

Haynes, C. T., Burgess, D., Camporeale, E., & Sundberg, T. (2015). Electron vortex magnetic cavities: A nonlinear coherent plasma structure. *Physics of Plasmas*, *22*, 012309.

Hellinger, P., & Stverak, S. (2018). Electron mirror instability: Particle-in-cell simulations. *Journal of Plasma Physics*, *84*, 905840402. https://doi.org/10.1017/S0022377818000703

Joy, S. P., Kivelson, M. G., Walker, R. J., Khurana, K. K., Russell, C. T., & Paterson, W. R. (2006). Mirror-mode structures in the Jovian magnetosheath. *Journal of Geophysical Research*, *111*, A12212. https://doi.org/10.1029/2006JA011985

Kivelson, M. G., & Southwood, D. J. (1996). Mirror instability II: The mechanism of nonlinear saturation. *Journal of Geophysical Research*, *101*, 17365–17371.

Li, J.-H., Yang, F., Zhou, X.-Z., Zong, Q.-G., Artemyev, A. V., Rankin, R., et al. (2020). Self-consistent kinetic model of nested electron- and ion-scale magnetic cavities in space plasmas. *Nature Communications*, *11*, 5616. https://doi.org/10.1038/s41467-020-19442-0

Liu, H., Zong, Q.-G., Zhang, H., Sun, W. J., Zhou, X.-Z., Gershman, D. J., et al. (2019a). The geometry of an electron scale magnetic cavity in the plasma sheet. *Geophysical Research Letters*, *46*, 9308–9317. https://doi.org/10.1029/2019GL083569

Liu, H., Zong, Q.-G., Zhang, H., Xiao, C. J., Shi, Q. Q., Yao, S. T., et al. (2019b). MMS observations of electron scale magnetic cavity embedded in proton scale magnetic cavity. *Nature Communications*, *10*, 1040. https://doi.org/10.1038/s41467-019-08971-y

Liu, J., Yao, S.-T., Shi, Q.-Q., Wang, X.-G., Zong, Q.-G., Feng, Y.-Y., et al. (2020). Electron energization and energy dissipation in microscale electromagnetic environments. *The Astrophysical Journal Letters*, *889*, 2. https://doi.org/10.3847/2041-8213/abab92

Marchand, R. (2010). Test-particle simulation of space plasmas. *Communications in Computational Physics*, *8*, 471–483. https://doi.org/10.4208/cicp.201009.280110a

Plaschke, F., Karlsson, T., Götz, C., Möstl, C., Richter, I., Volwerk, M., et al. (2018). First observations of magnetic holes deep within the coma of a comet. *Astronomy & Astrophysics*, *618*, A114. https://doi.org/10.1051/0004-6361/201833300

Pollock, C., Moore, T., Jacques, A., Burch, J., Gliese, U., Saito, Y., et al. (2016). Fast plasma investigation for magnetospheric multiscale. *Space Science Reviews*, *199*, 331–406. https://doi.org/10.1007/s11214-016-0245-4

Roytershteyn, V., Karimabadi, H., & Roberts, A. (2015). Generation of magnetic holes in fully kinetic simulations of collisionless turbulence. *Philosophical Transactions of the Royal Society A: Mathematical, Physical and Engineering Sciences*, *373*, 20140151. https://doi.org/10.1098/rsta.2014.0151

Russell, C. T., Riedler, W., Schwingenschuh, K., & Yeroshenko, Y. (1987). Mirror instability in the magnetosphere of comet Halley. *Geophysical Research Letters*, *14*, 644.

Shustov, P. I., Artemyev, A. V., Vasko, I. Y., & Yushkov, E. V. (2016). Kinetic models of sub-ion cylindrical magnetic hole. *Physics of Plasmas*, *23*, 122903. https://doi.org/10.1063/1.4972093

Shustov, P. I., Zhang, X.-J., Pritchett, P., Artemyev, A. V., Angelopoulos, V., Yushkov, E., & Petrukovich, A. A. (2019). Statistical properties of sub-ion magnetic holes in the dipolarized magnetotail: Formation, structure, and dynamics. *Journal of Geophysical Research: Space Physics*, *124*, 342–359. https://doi.org/10.1029/2018JA025852

Southwood, D. J., & Kivelson, M. G. (1993). Mirror instability: 1. Physical mechanism of linear instability. *Journal of Geophysical Research*, *98*, 9181–9187.

Sun, W. J., Shi, Q. Q., Fu, S. Y., Pu, Z. Y., Dunlop, M. W., Walsh, A. P., et al. (2012). Cluster and TC-1 observation of magnetic holes in the plasma sheet. *Annales Geophysicae*, *30*, 583–595. https://doi.org/10.5194/angeo-30-583-2012

Sundberg, T., Burgess, D., & Haynes, C. T. (2015). Properties and origin of subproton-scale magnetic holes in the terrestrial plasma sheet. *Journal of Geophysical Research: Space Physics*, *120*, 2600–2615. https://doi.org/10.1002/2014JA020856

Torbert, R. B., Russell, C. T., Magnes, W., Ergun, R. E., Lindqvist, P.-A., LeContel, O., et al. (2016). The FIELDS instrument suite on MMS: Scientific objectives, measurements, and data products. *Space Science Reviews*, *199*, 105–135. https://doi.org/10.1007/s11214-014-0109-8

Tsurutani, B. T., Lakhina, G. S., Verkhoglyadova, O. P., Echer, E., Guarnieri, F. L., Narita, Y., Constantinescu, D. O., et al. (2011). Magnetosheath and heliosheath mirror mode structures, interplanetary magnetic decreases, and linear magnetic decreases: Differences and distinguishing features. *Journal of Geophysical Research*, *116*, A02103. https://doi.org/10.1029/2010JA015913

Turner, J. M., Burlaga, L. F., Ness, N. F., & Lemaire, J. F. (1977). Magnetic holes in the solar wind. *Journal of Geophysical Research*, *82*, 1921–1924.

Winterhalter, D., Neugebauer, M., Goldstein, B. E., Smith, E. J., Bame, S. J., & Balogh, A. (1994). Ulysses field and plasma observations of magnetic holetongs in the solar wind and their relation to mirror-mode structures, *Journal of Geophysical Research*, *99*, 23371–23381, https://doi.org/10.1029/94JA01977

Xiao, T., Shi, Q. Q., Zhang, T. L., Fu, S. Y., Li, L., Zong, Q. G., et al. (2010). Cluster-C1 observations on the geometrical structure of linear magnetic holes in the solar wind at 1 AU. *Annales Geophysicae*, *28*, 1695–1702. https://doi.org/10.5194/angeo-28-1695-2010

Yao, S. T., Wang, X. G., Shi, Q. Q., Pitkänen, T., Hamrin, M., Yao, Z. H., et al. (2017). Observations of kinetic-size magnetic holes in the magnetosheath. *Journal of Geophysical Research: Space Physics*, *122*, 1990–2000. https://doi.org/10.1002/2016JA023858

Yao, S. T., Shi, Q. Q., Yao, Z. H., Guo, R. L., Zong, Q. G., Wang, X. G., et al. (2019). Electron mirror-mode structure: Magnetospheric multiscale observations. *The Astrophysical Journal Letters*, *881*, L31. https://doi.org/10.3847/2041-8213/ab3398

Yao, S. T., Hamrin, M., Shi, Q. Q., Yao, Z. H., Degeling, A. W., Zong, Q. G., et al. (2020). Propagating and dynamic properties of magnetic dips in the dayside magnetosheath: MMS observations. *Journal of Geophysical Research: Space Physics*, *124*, e2019JA026736. https://doi.org/10.1029/2019JA026736

Yao, S. T., Shi, Q. Q., Liu, J., Yao, Z. H., Guo, R. L., Ahmadi, N., et al. (2018). Electron dynamics in magnetosheath mirror-mode structures. *Journal of Geophysical Research: Space Physics*, *123*, 5561–5570. https://doi.org/10.1029/2018JA025607

Zhang, X.-J., Artemyev, A., Angelopoulos, V., & Horne, R. B. (2017). Kinetics of sub-ion scale magnetic holes in the near-Earth plasma sheet. *Journal of Geophysical Research: Space Physics*, *122*, 10304–10317. https://doi.org/10.1002/2017JA024197

Zhou, X.-Z., Angelopoulos, V., Runov, A., Liu, J., & Ge, Y. S. (2012). Emergence of the active magnetotail plasma sheet boundary from transient, localized ion acceleration. *Journal of Geophysical Research*, *117*, A10216. https://doi.org/10.1029/2012JA018171